Materials & Design 267 (2026) 116254

Contents lists available at ScienceDirect

Materials & Design

journal homepage: www.elsevier.com/locate/matdes

Directed gold nanoparticle synthesis with plasma-activated water

Jelena Štrbac [a,b], Damjan Vengust [a], Janez Zavašnik [a,b], James Leon Walsh [a,c], Uroš Cvelbar [a,b,*], Martina Modic [a,b,*], Vasyl Shvalya [a,b,*]

[a] Department of Gaseous Electronics (F6), Jožef Stefan Institute, Jamova cesta 39, SI-1000 Ljubljana, Slovenia
[b] Jožef Stefan International Postgraduate School, Jamova cesta 39, SI-1000 Ljubljana, Slovenia
[c] York Plasma Institute, School of Physics, Engineering and Technology, University of York, York YO10 5DD, UK

ARTICLE INFO

Keywords:
Gold nanoparticles
Plasma-activated water
Tuneable synthesis
Surfactant-free synthesis
Plasmonic nanoparticles

ABSTRACT

Plasma-activated water (PAW) enables surfactant-free synthesis of gold nanoparticles (AuNPs) at room temperature and acts as a reaction medium with tuneable reactive oxygen and nitrogen species (ROS and RNS), decoupled from the plasma discharge. Treating deionised water with an argon atmospheric-pressure plasma jet for 1–16 min increased H_2O_2 concentration from 0 to 8 mM, lowered pH from 7.0 to 3.5, and raised the oxidation–reduction potential from 0 to 400 mV, while maintaining negligible RNS levels. These changes directly influence Au^{3+} reduction and AuNP growth. At 1.00 mM [Au^{3+}], increasing PAW activation time from 1 to 16 min shortened the reduction time tenfold and shifted the LSPR maximum from 610 to 538 nm, with particle size decreasing from 120 nm to about 80 nm. Using the most reactive PAW (16 min), decreasing [Au^{3+}] from 1.00 to 0.10 mM reduced the mean AuNP size from 80 to 35 nm, yielding uniform, well-faceted nanoparticles. Weakly activated PAW (1–2 min) yields slower, partially incomplete reduction, broader size distributions, and more planar nanoparticles. These results establish PAW as a sustainable method for directed AuNP reduction kinetics, size, morphology, and optical response without external reducing or capping agents.

1. Introduction

Structurally complex polyhedral gold nanoparticles (AuNPs) exhibit enhanced plasmonic, catalytic, and electronic properties compared to spherical nanoparticles due to the presence of twin boundaries, lattice defects, and faceted surfaces that influence chemical sensitivity and interactions with external electric fields [1,2]. Such structural features are particularly important for applications involving plasmonic sensing, catalysis, and surface-enhanced spectroscopies, controlled design for functional biomedical and antibacterial platforms, theragnostic and therapeutic devices in clinical trials, where nanoparticle morphology and crystallographic complexity strongly affect performance [3–6]. However, obtaining structurally complex AuNPs in a controlled and reproducible manner remains a challenge for many physically driven synthesis methods, including ablation and sputtering approaches, whereas chemical routes offer greater flexibility in tailoring nanoparticle morphology and structural properties required for tuneable optical and plasmonic behaviour [2].

Conventional chemical routes such as the Turkevich [7] and Brust–Schiffrin [8] methods typically yield relatively low-defect polycrystalline AuNPs with limited control over twin preservation, defect density, and anisotropic growth, producing predominantly quasi-spherical particles. Although subsequent polymer- [9] or biomolecule-assisted [10] modifications have partially improved size uniformity and colloidal stability, they still offer limited influence over internal crystallinity and shape evolution. To achieve structural control, many established synthesis strategies rely on chemical reductants, stabilisers, and surface-directing agents, including sodium borohydride, hydrazine-based reductants, poly(vinylpyrrolidone), and cetyltrimethylammonium bromide [7–10]. While effective in directing nanoparticle growth, these additives introduce additional chemistry that may become undesirable in medicine, biotechnology, catalysis, and sensing applications where chemically clean nanoparticle surfaces are required.

Recently, non-thermal plasma-assisted synthesis has emerged as a rapid, tuneable, and environmentally benign route for the generation of gold nanostructures. Many plasma-based methods rely on solution plasma processing across gas–liquid interfaces, where precursor solutions interact with plasma-generated reactive species. These systems facilitate plasma-driven electrochemical reactions, enabling Au^{3+}

* Corresponding authors at: Department of Gaseous Electronics (F6), Jožef Stefan Institute, Jamova cesta 39, SI-1000 Ljubljana, Slovenia.
E-mail addresses: uros.cvelbar@ijs.si (U. Cvelbar), martina.modic@ijs.si (M. Modic), vasyl.shvalya@ijs.si (V. Shvalya).

https://doi.org/10.1016/j.matdes.2026.116254
Received 13 February 2026; Received in revised form 17 May 2026; Accepted 17 May 2026
Available online 18 May 2026

reduction and nanoparticle synthesis without additional reducing agents, organic solvents, or prolonged thermal exposure [11–23]. Such approaches have demonstrated a degree of control over nanoparticle size and morphology together with the possibility for simultaneous surface functionalisation.

However, direct plasma–liquid synthesis still faces several limitations associated with coupled plasma–reaction environments, including small reaction volumes, solvent evaporation, fluctuations in reagent concentration and pH, as well as local thermal effects in both plasma and liquid phases. The outcome of nanoparticle synthesis is highly sensitive to reactive species flux, gas flow dynamics, discharge power, and plasma–liquid interaction geometry, together with numerous system-specific parameters that can compromise reproducibility and scalability. In addition, direct plasma exposure continuously modifies the reaction medium during nanoparticle nucleation and growth, making it difficult to establish systematic relationships between plasma-generated chemistry and nanoparticle formation pathways [24].

These limitations can be addressed using a temporally decoupled two-step strategy in which plasma treatment is separated from nanoparticle synthesis. Instead of direct plasma exposure of an aqueous gold precursor solution during nanoparticle formation, only deionized water is first exposed to atmospheric-pressure plasma and subsequently used as the reaction medium. During plasma treatment, energy and reactive species are transferred across the gas–liquid interface, generating a dynamic mixture of reactive oxygen and nitrogen species (RONS), including short-lived radicals (OH, NO, $ONOO^-$) and longer-lived molecular species (H_2O_2, O_3, NO_2^-, NO_3^-) (**Table S1**). These species alter the physicochemical properties of water by lowering pH, increasing oxidation–reduction potential, balancing ROS and RONS interplay and enhancing conductivity [25–28]. Plasma-activated water has been extensively investigated for food preservation, surface functionalisation, agriculture, and microbial inactivation, demonstrating effectiveness and chemical stability under diverse operating conditions [29–31]. The balance between ROS and RONS species can be adjusted through plasma design and operating conditions, enabling control over PAW chemistry [32]. Beyond these established applications, plasma-activated water can also serve as a reactive liquid medium for Au^{3+} reduction and surfactant-free AuNP synthesis (**Table S2**). Unlike conventional wet-chemistry approaches that rely on molecular reductants or capping agents, the present approach uses the chemical state of plasma-activated water itself to influence nanoparticle growth and morphology through changes in reactive oxygen species balance, pH, and redox conditions.

Despite increasing interest in plasma-assisted AuNP synthesis, a systematic understanding of how the chemical state of plasma-activated water influences Au^{3+} reduction kinetics, nanoparticle growth pathways, and resulting morphology remains limited. In particular, systematic correlations between reactive species composition, pH, redox conditions, and the resulting nanoparticle size, morphology, and plasmonic characteristics have not yet been clearly established. Establishing such correlations is important for the design of gold nanomaterials where morphology and structural complexity are influenced by liquid-phase reaction conditions rather than conventional chemical additives. In this study, an atmospheric-pressure argon plasma jet was used for treatment of deionized water and generation of plasma-activated water with physicochemical properties tuned through variation of the plasma treatment time. The resulting plasma-activated water was subsequently used for room-temperature synthesis of gold nanoparticles at Au^{3+} precursor concentrations between 0.10 and 1.00 mM. By correlating plasma-activated water chemistry with Au^{3+} reduction kinetics, plasmonic response, and nanoparticle morphology, the study examines how plasma-generated reactive oxygen species influence nanoparticle growth and faceting under surfactant-free conditions.

2. Materials and methods

2.1. Plasma setup and preparation of plasma-activated water

The atmospheric-pressure plasma jet (APPJ) system was designed in-house (Fig. 1a). A high voltage (~12 kV, ~20 kHz) was applied to a 0.2 mm gold electrode positioned inside a quartz tube (6 mm outer diameter, tapered to 2 mm at the nozzle) through which argon flowed at 0.5 L min^{-1}. The gas flow was initiated 1 min prior to plasma ignition to purge residual air from the reactor. The nozzle-to-liquid distance was approximately 1 mm. Plasma was generated due to the intense localized electric field at the wire tip. The tube was positioned vertically above the water surface in a glass vial placed on a grounded metal stand, serving as a counter electrode via capacitive coupling. Voltage and current waveforms were recorded using an oscilloscope (MSO5000, Rigol) equipped with a high-voltage probe (P6015A, Tektronix) and a current probe (2877, Pearson Electronics). Ultrapure water (3 mL) was treated with the APPJ for 1, 2, 4, 8, or 16 min to generate plasma-activated water (PAW), referred to as PAW:1, PAW:2, PAW:4, PAW:8, and PAW:16, respectively. Following plasma treatment, the samples were stabilized on ice for approximately 1 h prior to further use.

2.2. Optical emission spectroscopy

Optical emission spectroscopy (OES) measurements were performed in situ during plasma treatment using a quartz cuvette to improve transmission below 350 nm. Plasma emission was collected using an optical fibre positioned at the plasma–liquid interface and connected to a spectrograph (Shamrock SR500i-D2-R, Andor) equipped with an iCCD detector (iStar 334 T CCD, Andor). Broad spectral scans were acquired in the 250–850 nm range using a 300 lines mm^{-1} grating, while high-resolution measurements in the OH region (306–312 nm) were performed using a 2400 lines mm^{-1} grating. Synthetic OH spectra used for rotational temperature estimation were generated using the LIFBASE simulation software.

2.3. Physicochemical characterization of PAW

The concentrations of reactive oxygen and nitrogen species in PAW were determined using established analytical assays. Hydroxyl radicals ($^{\bullet}OH$) were quantified using terephthalic acid as a fluorescent probe through formation of 2-hydroxyterephthalic acid ($\lambda ex/em = 310/425$ nm) [33]. Hydrogen peroxide concentration was determined using the ferrous oxidation–xylenol orange method [34]. Nitrite concentration was measured using the Griess reagent system (Promega, Madison, WI, USA), while nitrate concentration was determined spectrophotometrically at 210 nm [35]. The pH and oxidation–reduction potential (ORP) of PAW samples were measured using a SevenExcellence pH meter (Mettler Toledo) equipped with the corresponding electrodes immersed directly into the samples.

Cyclic voltammetry measurements were performed using a Gamry 5000 Interface potentiostat and Gamry Framework software. Platinum working and counter electrodes together with an Ag/AgCl reference electrode were immersed in an electrochemical cell containing 20 mL of analyte. Measurements were conducted in the potential range from −0.6 to 1.0 V using a scan rate of 100 mV s^{-1}, step size of 10 mV, and five consecutive cycles. The obtained data were analyzed using Gamry Echem Analyst software.

2.4. Gold nanoparticle synthesis and UV–Vis monitoring

A 10 mM aqueous $AuCl_3$ stock solution was prepared by dissolving $AuCl_3$ salt (99.9%, Thermo Scientific) in ultrapure water (OmniaPure system, Stakpure, Germany). Final reaction mixtures were prepared in a total volume of 1 mL by mixing appropriate aliquots of the $AuCl_3$ stock solution with PAW samples to obtain final Au^{3+} concentrations of 0.10,

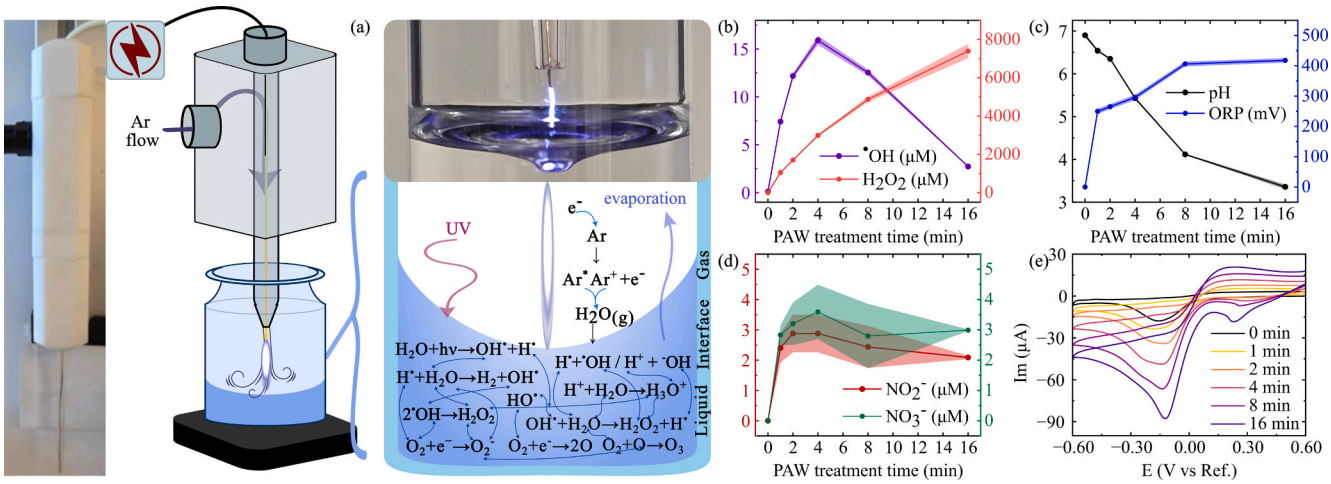

Fig. 1. Generation and physicochemical characterization of plasma-activated water (PAW). (a) Photograph and schematic of the gas–liquid argon plasma jet (APPJ) setup with an Au wire inside a glass tube connected to a high-voltage generator, showing gas flow direction, plasma–liquid interaction, and key reactive species formation pathways, with an inset photograph of the experimental setup. (b) Evolution of $^{\bullet}OH$ and H_2O_2 concentrations as a function of treatment duration. (c) Variation of pH and oxidation–reduction potential (ORP) with treatment time. (d) Concentrations of NO_2^- and NO_3^- formed in PAW. (e) Cyclic voltammograms recorded for PAW after different treatment times. Shaded areas in (b–d) represent standard deviations from three independent measurements.

0.25, 0.50, and 1.00 mM. The reduction process and nanoparticle formation were monitored using UV–Vis spectroscopy. Spectra of 300 μL aliquots placed in microtiter plates were recorded using a Spark 10 M microplate reader (Tecan) in the 250–800 nm range. Measurements were acquired every 10 min for 5 h. Spectral evolution in the 250–350 nm region was associated with Au^{3+} precursor reduction, while the emergence of localized surface plasmon resonance (LSPR) bands in the visible region was used to monitor AuNP formation [36–38].

2.5. Nanoparticle characterization

Particle size distributions and particle concentrations were analyzed using multi-angle dynamic light scattering (MADLS) performed on a Zetasizer Ultra instrument (Malvern Panalytical) equipped with a 633 nm He–Ne laser. Measurements were carried out using 1 mL samples loaded into disposable cuvettes (DTS0012) at 25 °C. Individual MADLS acquisitions lasted approximately 200 s [39]. Scanning electron microscopy (SEM) was performed using a Verios 4G HP microscope (Thermo Fisher Scientific, USA) operated at 5–20 kV. Transmission electron microscopy (TEM) and scanning transmission electron microscopy (STEM) analyses were conducted using a Talos 200X G2 microscope (Thermo Fisher Scientific, USA) operated at 200 kV. Bright-field (BF) and dark-field (DF) detectors were employed for structural characterization. SEM samples were prepared by drop-casting colloidal dispersions onto silicon wafers, while TEM samples were prepared by depositing diluted colloidal dispersions onto carbon-coated copper grids followed by drying under ambient conditions. Quantitative morphometric analysis was performed using SEM and TEM micrographs of well-dispersed nanoparticles. Individual particles were manually outlined in Inkscape and subsequently analyzed in ImageJ to determine particle dimensions and geometric parameters. Approximately 330 ± 20 nanoparticles were analyzed per sample. Statistical processing and visualization were performed using OriginPro 2024b (OriginLab Corporation, USA).

3. Results and discussion

3.1. Optical emission spectroscopy of the plasma discharge

Optical emission spectroscopy (OES) measurements (**Fig. S1 b-c**) revealed strong OH emission at ~ 309 nm together with Ar lines in the 700–810 nm region and weaker H_β/H_α (486.1/656.3 nm) and O (777 nm) emission, while no nitrogen-band emission was observed after Ar purging. These spectral features are consistent with our previous characterization [40] of the same pin-based argon plasma configuration, despite the lower Ar flow used here (500 vs 1500 sccm), and support a ROS-dominated discharge chemistry. Fitting of the OH(A–X) OES band in analogous manner to Olenik et al. [40] gave an approximate rotational temperature of T_{rot} ~ 900 K in the present case.

3.2. Physicochemical evolution of plasma-activated water

Upon plasma–liquid contact, a complex chemical interface is established, enriched by local electric fields and ultraviolet radiation. Transient species such as hydroxyl radicals ($^{\bullet}OH$) and superoxide anions (O^{2-}) coexist with longer-lived molecules including hydrogen peroxide (H_2O_2) and ozone (O_3). These species penetrate the liquid phase, where they engage in further reactions such as solvation, charge transfer, and radical recombination, leading to additional ROS formation in the bulk aqueous phase (**Table S1**). The dissociation of water also contributes, generating H^+ and OH^- ions that modulate pH and conductivity [25,41]. Although the behaviour of solvated electrons remains incompletely understood, they are presumed to undergo recombination or participate in subtle redox dynamics [42,43]. Overall, plasma-activated water (PAW) is a dynamic yet tuneable non-equilibrium medium characterized by continuous generation, transformation, and decay of reactive intermediates, as illustrated in Fig. 1a. To ensure reproducibility, PAW samples were left to stabilise for about an hour at low temperature prior to use, enabling the reactive composition to reach equilibrium while minimising contributions from short-lived or thermally induced species. Quantitative analysis of ROS, pH, ORP, and electrochemical behaviour revealed distinct temporal trends governed by species lifetime and plasma treatment duration (Fig. 1b–e). Similar temporal changes in PAW composition have been reported in previous dielectric-barrier-discharge studies.[44] In our case, hydroxyl radical generation during plasma treatment (Fig. 1b, purple), increased sharply at short treatment times (≈ 4 min, peak concentration of 15 μM) followed by a decline due to recombination into H_2O_2. After 16 min of plasma treatment, $^{\bullet}OH$ levels approached the detection limit, reflecting the clear transient nature of PAW from short- to long-lived species, prioritizing H_2O_2 accumulation. In contrast, all other species, including H_2O_2, pH, and ORP, were measured in rested PAW samples. The H_2O_2 concentrations (Fig. 1b, **red**) steadily increased with treatment time through $^{\bullet}OH$ recombination under acidic conditions, reaching 7–8 mM levels after 16 min of treatment and accompanied by a decrease in pH (Fig. 1c,

black) that stabilised after approximately 4 min. This evolution is reflected in the oxidation–reduction potential ORP (Fig. 1c, **blue**), which increases sharply and plateaus around 400 mV after 8 min of treatment. The positive ORP indicates that rested PAW is shifted toward an overall oxidising redox balance; however, a positive ORP does not preclude Au^{3+} reduction in PAW systems, where oxidative and reductive pathways may operate simultaneously. Accordingly, ORP is treated here as a relative descriptor of the overall redox state of PAW rather than a direct measure of reducing capacity [45]. Notably, PAW chemistry is strongly source-dependent. For instance, Tephiruk et al. generated PAW containing both ROS and RNS, with pH dropping to approximately 2.5 within 10 min and, after 60 min, H_2O_2 and NO_3^- reaching ~ 2.1 mM and 8.1 mM, respectively [46]. In contrast, the present Ar APPJ generates a predominantly ROS-rich PAW after 16 min, with H_2O_2 up to 7–8 mM. These differences underline that PAW composition depends strongly on source design, working gas, discharge conditions, treatment time, and gas–liquid coupling, which also define the exact requirements PAW must meet for certain tasks [47,48]. Only trace amounts (< 5 μM) of RNS (NO_2^- and NO_3^-) were detected in PAW (Fig. 1d), consistent with the idea that pre-blowing the vial suppresses their formation. This is a direct consequence of using argon as the feeding gas for the atmospheric-pressure plasma jet (APPJ), which efficiently displaces air from the reaction vial, leaving only trace amounts of residual nitrogen available for RNS generation.

Electrochemical measurements further support this view. Cyclic voltammetry (Fig. 1e) shows a gradual increase in redox activity with extended plasma exposure, along with broader and more pronounced peaks characteristic of accumulated long-lived species. The cathodic onset shifts toward less negative potentials with treatment time, indicating altered electron-transfer behaviour and a chemically more reactive redox environment [49,50]. Together, the trends in ROS concentration, H_2O_2 accumulation, pH decrease, and ORP evolution demonstrate that prolonged plasma treatment produces a progressively more reactive redox medium for Au^{3+} material.

The measured changes in PAW composition with increasing plasma treatment time indicate progressively stronger activation of the reaction medium. In particular, progressive plasma treatment transforms rested PAW from a weakly reactive medium into an acidic peroxide-rich reaction medium, with H_2O_2 increasing to 7–8 mM, pH decreasing to 3–4, and ORP rising to approximately 400 mV, while RNS remain below 5 μM and are therefore about three orders of magnitude lower than H_2O_2. These compositional changes suggest that nanoparticle synthesis in weakly and strongly activated PAW proceeds under different kinetic regimes. Weakly activated PAW may favour slower precursor conversion, delayed nucleation, and prolonged growth, whereas strongly activated PAW promotes rapid precursor conversion, burst nucleation, and formation of a larger number of nuclei, resulting in smaller and more uniform AuNPs. Although H_2O_2 is commonly regarded as an oxidant, it is redox-amphoteric and, in acidic chloride-containing media, can also act as a reductant towards ionic Au(III) [23,51]. Under these conditions, chloride-complexed Au(III) oxidises H_2O_2 to O_2 while being reduced to Au(0), because the $AuCl_4^-$/Au redox couple is highly noble ($E^\circ \approx +1.00$ V vs SHE). A plausible net pathway is therefore:

$$2AuCl_4^- + 3H_2O_2 \rightarrow 2Au^0 + 3O_2 + 6H^+ + 8Cl^-$$

3.3. Reduction kinetics of Au^{3+}: Influence of PAW activation time and precursor concentration

The influence of PAW activation time and precursor concentration on Au^{3+} reduction kinetics was evaluated using time-resolved UV–Vis spectroscopy. The gradual decrease of the absorption band between 250–350 nm, a characteristic of ligand-to-metal charge transfer in the $[AuCl_3(OH)]^-$ complex, signifies the progression of the reduction (Fig. 2a) [37]. Data extracted using the local intensity maxima across the 250–350 nm range, obtained from UV–Vis spectra (**Fig. S2**), illustrate how the time required for complete reduction depends both on the initial concentration of gold ions and on the duration of PAW treatment (Fig. 2b).

Longer plasma treatment times increased the chemical reactivity and redox turnover of PAW, resulting in faster and more efficient reduction of Au^{3+}. In particular, PAW:16 reduced 0.10 mM [Au^{3+}] almost instantaneously and completed the reduction of 1.00 mM within 10 min. Time-resolved photographs confirmed the characteristic colour evolution from colourless to deep pink, consistent with rapid formation of colloidal AuNPs (Fig. 2c) [52]. The observed reduction behaviour was reproducible across independently prepared samples under identical conditions.

3.4. Effect of PAW activation time on AuNP formation and morphology

Consecutive UV–Vis absorbance scans provide insight into the dynamics of AuNP formation, with the plasmonic band gradually emerging in the 450–700 nm range as reduction proceeds. The evolution and eventual stabilisation of this band mark the reaction's progression and completion, as evidenced by the overlap of consecutive spectra indicating a stable colloidal state. Once stabilisation was achieved, the samples were further characterised by multi-angle dynamic light scattering (MADLS) to assess particle size distributions and by electron microscopy to examine morphology and structure. To disentangle the

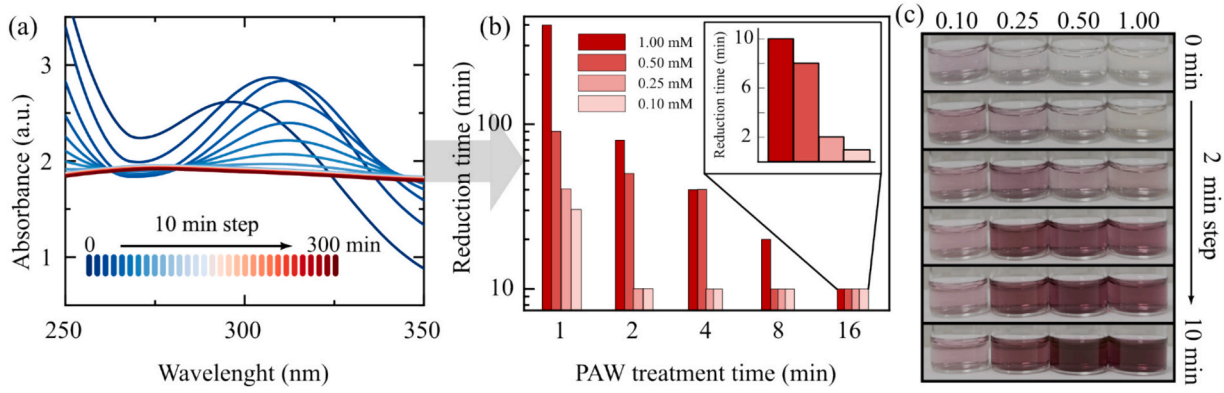

Fig. 2. Reduction of Au^{3+} by PAW. (a) Representative UV–Vis spectra showing a progressive decrease of the Au^{3+} absorption band in the 250–350 nm region over time. (b) Reduction times extracted from the UV–Vis spectra for PAW samples treated for 1–16 min with different Au^{3+} precursor concentrations (0.10, 0.25, 0.50, and 1.00 mM). (c) Photographs showing the development of the ruby-red colour characteristic of colloidal gold nanoparticles, corresponding to samples prepared with 16 min PAW and different precursor concentrations (0.10–1.00 mM). (For interpretation of the references to colour in this figure legend, the reader is referred to the web version of this article.)

effects of PAW reactivity and precursor availability, two representative cases are discussed (full dataset in Supplementary Information, Fig. S3–S6): (i) varying PAW treatment time at a fixed [Au^{3+}] = 1.00 mM, and (ii) applying the most reactive PAW (PAW:16) across a range of precursor concentrations (0.10–1.00 mM).

For the first case, UV–Vis spectra consistently exhibited plasmonic bands between 540 and 600 nm, confirming colloidal nanoparticle formation (Fig. 3a). Following exposure to PAW:8 and PAW:16 plasmonic bands rapidly appeared and stabilised, while shorter treatment times (1–2 min) resulted in slower stabilisation (>1h), with plasmon maxima located at longer wavelengths. Comparison of Au^{3+} reduction progress (Fig. S2) with plasmonic band evolution (Fig. S3) reveals that weaker PAW (e.g., PAW:1, 1.00 mM) is unable to fully reduce the precursor at high concentrations, resulting in delayed nucleation and prolonged growth. In contrast, PAW treated for ≥ 8 min promotes rapid burst nucleation, consistent with a high flux of kinetically accessible reducing intermediates under acidic conditions. Although ORP increases with plasma exposure, it should be interpreted here as an integrated descriptor of the evolving redox environment rather than a direct driving force for reduction. The combination of elevated H_2O_2 concentration, low pH, and non-equilibrium ROS chemistry accelerates Au^{3+} consumption relative to particle growth, leading to uniform nucleation and controlled morphology. Key characterisation parameters, including plasmonic band position, stabilisation time, nanoparticle mean hydrodynamic size, and concentration from MADLS (Fig. S4a, b), are summarised in Table 1. MADLS analysis shows particle sizes ranging from 70 to 120 nm with normal size distributions and increasing particle concentrations, from approximately 10^8 particles/mL for PAW:1 to 10^{10} particles/mL for PAW:16 (Fig. S4a, b). Samples prepared with weaker PAW (1–2 min) exhibit broader distributions and occasional formation of larger anisotropic particles, consistent with UV–Vis signatures. These observations are further supported by SEM analysis (Fig. 3b), which reveals uniform, compact faceted morphologies for samples treated with PAW:4–16, while weaker PAW (1–2 min) produces a heterogeneous population comprising both faceted nanoparticles and larger 2D platelike structures. The evolution and stabilisation of the LSPR band were consistent across repeated syntheses performed under identical conditions. Collectively, these results indicate that stronger, more acidic PAW promotes faster Au^{3+} consumption and burst nucleation, thereby limiting prolonged growth and reducing morphological dispersion. Under these conditions, the ligand-free acidic medium and plasma-defined redox chemistry are also consistent with mild selective restructuring or etching of high-energy growth motifs, which can favour the formation of compact, well-faceted nanoparticles.

Table 1
Characterization of AuNPs for 1.00 mM [Au^{3+}] concentration with different PAWs.

Parameter	1 min		2 min	4 min	8 min	16 min
LSPR band (nm)	611 ± 10		564 ± 6	550 ± 4	548 ± 3	548 ± 3
Stabilization (min)	100		80	30	10–20	10–20
Size (nm)	120 ± 15	325 ± 30	95 ± 7	85 ± 6	82 ± 5	80 ± 5
Concentration (p/ml)	2-3·10^8	1-2·10^6	8-9·10^8	6-7·10^9	1-2·10^{10}	1-2·10^{10}

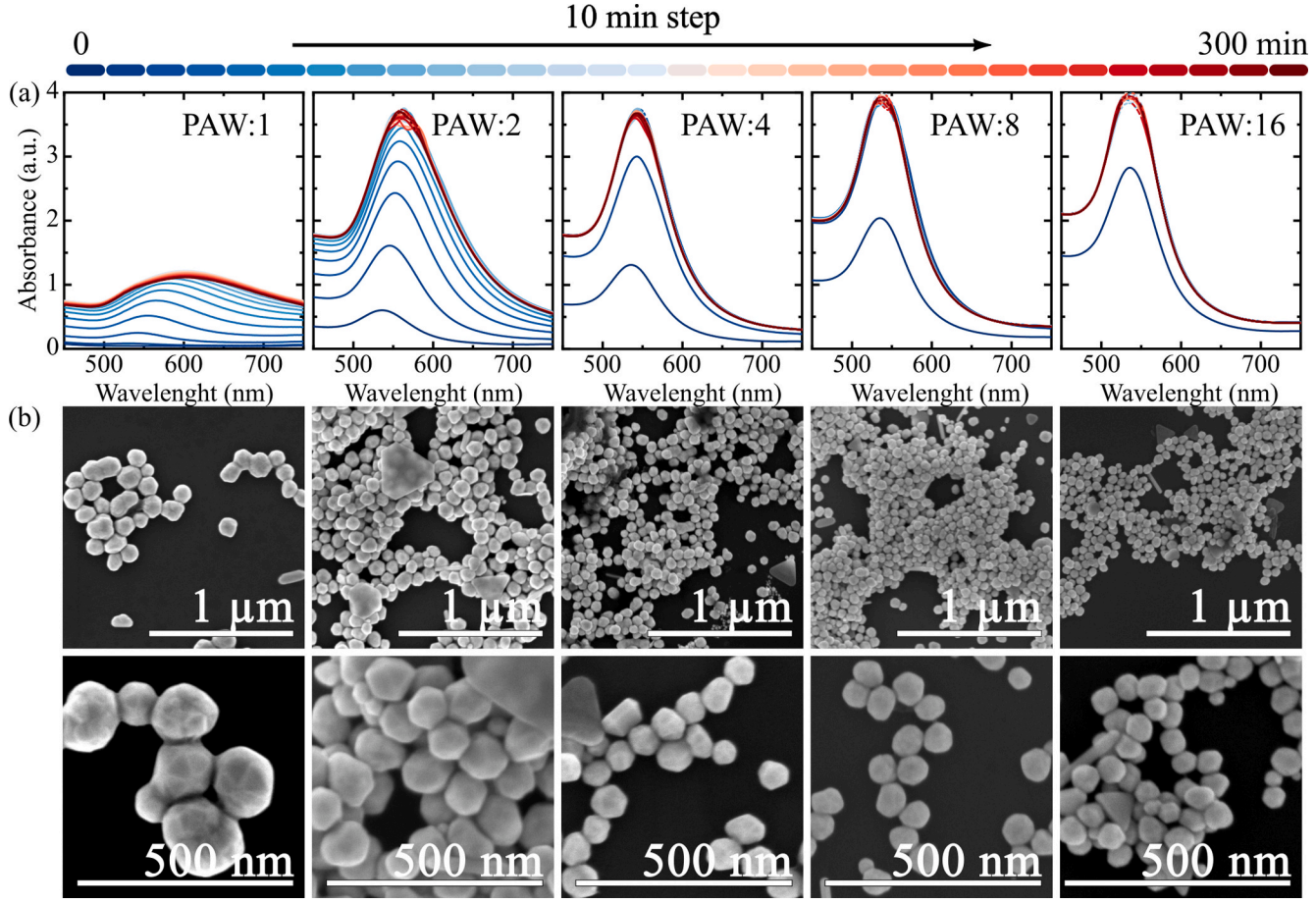

Fig. 3. (a) Evolution of the LSPR absorption peak in representative operando UV–Vis spectra (10 min step between 2 neighbouring spectra) of 1.00 mM [Au^{3+}] reduced with PAW samples treated for 1, 2, 4, 8, and 16 min. (b) Corresponding SEM micrographs of the resulting AuNPs, collected on the day of synthesis.

3.5. Effect of [Au^{3+}] precursor on AuNP growth

For the second case, designed to examine how precursor concentration influences nanoparticle morphology, the strongest PAW:16 was challenged with varying concentrations of Au^{3+} precursor, ranging from 0.10 to 1.00 mM. Normalised UV–Vis spectra (Fig. 4a) displayed distinct plasmonic bands between 450 and 700 nm, shifting progressively toward longer wavelengths with increasing [Au^{3+}], consistent with the formation of larger nanoparticles. Complementary MADLS (Fig. 4b) analysis revealed an increase in average particle size from approximately 40 to 80 nm, while particle concentrations remained within the same order of magnitude (around 10^9 particles/mL) across all samples. This indicates that initial nucleation density is largely conserved under these conditions, producing a comparable number of initial nuclei. At lower precursor concentrations, the limited amount of available material restricts subsequent growth, yielding smaller particles; whereas at higher concentrations, additional material deposition promotes extended growth and the formation of larger ones. The process proved reproducible, as confirmed by three independent replicate samples that showed comparable particle sizes and concentrations over time (**Fig. S5, samples A, B, C**), while the resulting colloids remained stable. Zeta potential measurements further confirmed colloidal stability, with ζ-potential values ranging from approximately − 23 to − 33 mV depending on [Au^{3+}] (**Table S3**). The negative surface charge together with the acidic, ion-rich reaction medium likely contributes to electrostatic stabilization of the surfactant-free AuNP dispersions over the monitored period [53].

3.6. Structural characterization and statistical analysis of AuNP morphology

SEM and TEM analyses reveal that PAW-mediated synthesis favours polyhedral and faceted morphologies over spherical particles, distinct from the classical Turkevich synthesis route (Fig. 4c–e). The TEM survey (Fig. 4d-e **and Fig. S6-7**) indicates that most particles adopt polyhedral shapes, while a smaller fraction form anisotropic two-dimensional structures such as rods and triangular or hexagonal plates. The overall population also includes undistorted face-centred cubic cuboctahedra, polycrystalline clusters, and multiply twinned Platonic-like solids, such as dodecahedra and icosahedra. The proportion of plate-like particles decreases with longer PAW activation, resulting in more symmetric morphologies composed of multiple crystalline domains and distinct twinned configurations. Such polyhedral and multiply twinned structures are typically associated with rapid nucleation, high local supersaturation, and subsequent coalescence or restructuring of small triangular or twinned seeds into more compact Platonic-like forms [11]. Representative BF-STEM and DF-STEM micrographs (Fig. 5) further support this interpretation, showing that particles prepared from PAW:16 at 1.00 mM Au^{3+} are larger and exhibit stronger internal contrast and faceting, whereas the 0.10 mM sample remains smaller and more uniform. These observations are consistent with previous electron microscopy studies of anisotropic and structurally heterogeneous AuNPs [11,54]. Such structural and morphological diversity may be relevant for catalytic and plasmonic applications, where particle anisotropy and faceting influence surface and optical properties [1,40] (see Table 2).

A puzzling feature appeared in the MADLS data (Fig. 4b) for 0.10 and

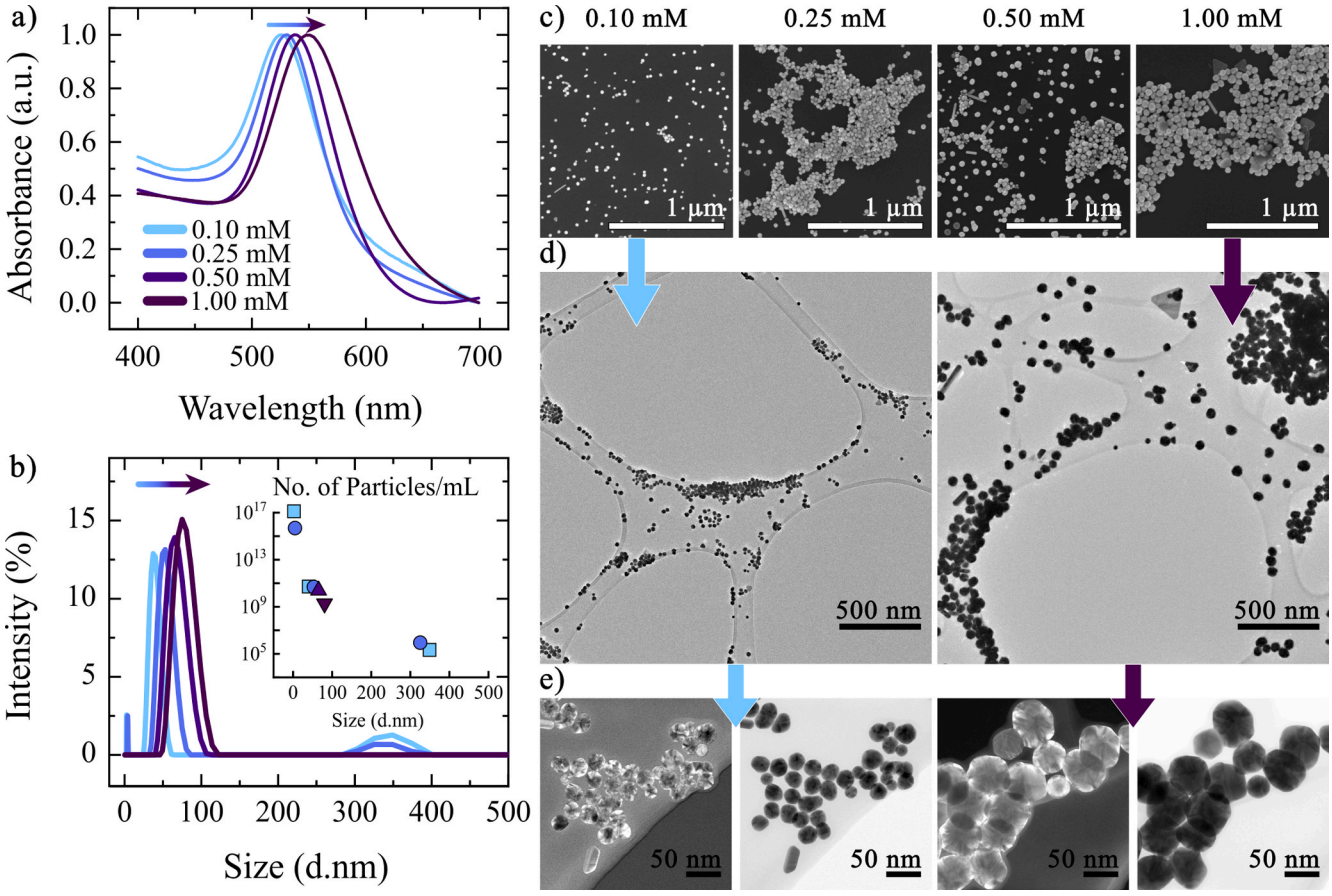

Fig. 4. Effect of Au^{3+} concentration on the optical and morphological properties of AuNPs synthesized using PAW:16. (a) Normalized UV–Vis spectra showing a gradual LSPR redshift with increasing [Au^{3+}]. (b) MADLS size distributions with an inset of particle concentration. (c) SEM micrographs illustrating the particle morphology. (d) TEM and (e) STEM (dark-field and bright-field mode) micrographs of AuNPs synthesized at 0.10 and 1.00 mM, revealing pronounced differences in NP size and their well-defined faceting.

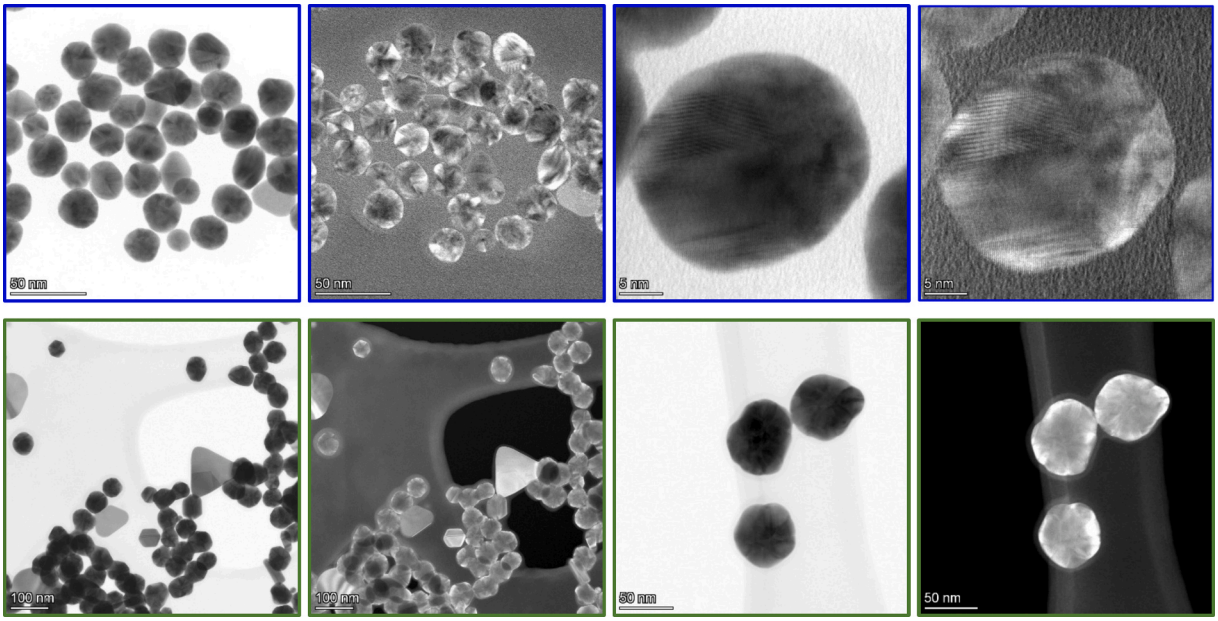

Fig. 5. Representative BF-STEM (bright-field) and DF-STEM (dark-field) TEM micrographs of AuNPs synthesized using PAW:16 at 0.1 mM Au^{3+} (blue boxes, top row) and 1.0 mM Au^{3+} (green boxes, bottom row). (For interpretation of the references to colour in this figure legend, the reader is referred to the web version of this article.)

Table 2
Characterization of AuNPs for 0.10–1.00 mM [Au^{3+}] with PAW:16. Stabilization time was extracted by monitoring LSPR position and intensity from UV–Vis with 2 min step between neighbouring spectra).

Parameter	0.10 mM	0.25 mM	0.50 mM	1.00 mM
Plasmonic band (nm)	525 ± 2	530 ± 2	538 ± 3	548 ± 3
Stabilization time (min)	2	2	4	8
Size (nm)	35 ± 3	50 ± 3	65 ± 4	80 ± 5
Concentration (p/ml)	$4\text{-}5{\cdot}10^{10}$	$6\text{-}7{\cdot}10^{10}$	$2\text{-}3{\cdot}10^{10}$	$1\text{-}2{\cdot}10^{10}$

0.25 mM, showing signals corresponding to apparent ultrasmall species detected in excessively high concentrations (2–4 nm, 10^{15}–10^{17} particles/mL) alongside a small fraction of larger particles (~350 nm, 10^{4} particles/mL). While the latter likely arise from 2D anisotropic morphologies observed by SEM, TEM analysis did not reveal any sub-5 nm particles that could explain the unrealistically high particle counts inferred from MADLS. To resolve this, the total particle volume estimated from MADLS data was compared with the theoretical mass balance. Following the spherical-geometry assumption inherent to MADLS, the total nanoparticle volume at 0.10 mM was estimated to exceed the theoretical maximum by roughly 28600% (Table S4), a physically

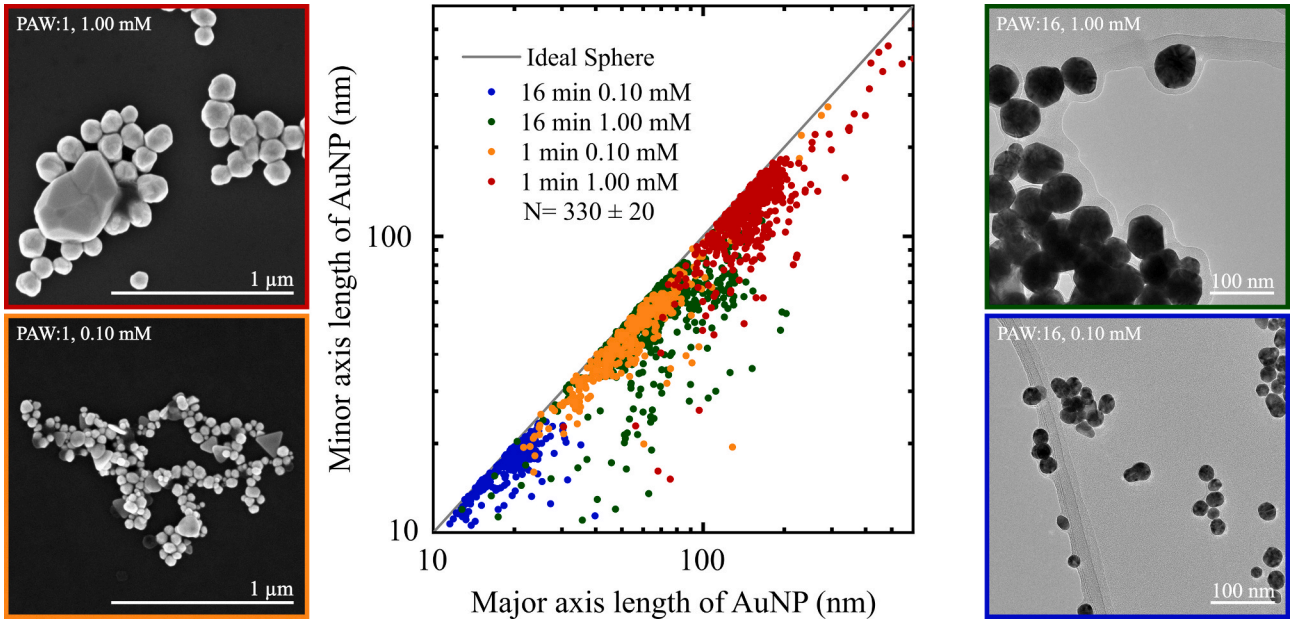

Fig. 6. Statistical representation of the average size and shape of AuNPs synthesized under different PAW conditions. Each point corresponds to one AuNP, plotted by its major and minor axis lengths. The grey line indicates the ideal spherical shape (1:1 ratio). The data illustrate the systematic variation in particle anisotropy with PAW duration (1 or 16 min) and $AuCl_3$ concentration (0.10 or 1.00 mM). Representative SEM (left) and TEM (right) micrographs correspond to the colour-coded data sets.

implausible result. This finding confirms that the apparent ultrasmall population is not real but an artefact. Similar false peaks have been reported for non-spherical particles, where deviations from round shape cause the instrument to misinterpret scattering intensity.[55] These results demonstrate that the additional MADLS peaks are artefactual and arise from non-spherical scattering behaviour, consistent with the faceted morphology of the synthesized AuNPs. These artifacts primarily affect the absolute particle concentration derived for the ultrasmall population (< 5 nm) by adding an additional size population, but do not alter the overall trend in hydrodynamic size as cross-checked by TEM. Accordingly, the MADLS results are interpreted here as qualitative support for size evolution across the sample series rather than as a quantitative measure of absolute nanoparticle number in the artifactual sub-5 nm regime, and can be used to refine commercially available DLS software.

Statistical evaluation of 325 ± 20 AuNPs per sample (Fig. 6) supports these observations. Together with the independent repeat measurements of PAW properties and the replicate colloid stability data, this provides the statistical and experimental basis for the trends discussed below. Most data points cluster close to the 1:1 line, indicating predominantly isotropic, compact polyhedral shapes. For weaker PAW (PAW:1), the points are more dispersed within each group, reflecting less uniform growth and a broader particle size distribution. In samples synthesized at higher [Au^{3+}] (1.00 mM), the data deviate further from the 1:1 line, suggesting a wider variety of particle morphologies enabled by the increased availability of precursor material. In contrast, stronger PAW (PAW:16) yields more uniform and sharply faceted AuNPs, with anisotropic species representing less than 7% of the total population.

Taken together, the chemistry and morphology data indicate that PAW-mediated AuNP formation is governed primarily by reaction kinetics rather than by a change in the overall Au(III)-to-Au(0) chemistry. At 1.00 mM [Au^{3+}], increasing PAW activation accelerates precursor reduction, shifts the LSPR to shorter wavelengths, and decreases the mean particle size; under PAW:16, lowering [Au^{3+}] decreases the particle size further. In this sense, weakly activated PAW acts as a mild-reduction pathway, functionally analogous to citrate-based Turkevich chemistry, whereas strongly activated PAW approaches faster reduction conditions with higher transient supersaturation, more comparable to Brust-type synthesis. Under such rapid nucleation conditions, the formation of anisotropic or morphologically diverse seeds, followed by coalescence, overgrowth, or restructuring into more compact particles, is consistent with reported growth pathways of anisotropic and multiply twinned gold nanostructures. [8,56] Importantly, the resulting particles are not predominantly spherical but increasingly polyhedral and faceted, in agreement with the SEM, TEM and STEM observations. Unlike both classical routes, however, plasma-treated PAW enables access to these synthesis conditions at room temperature and under surfactant-free conditions. We therefore interpret the observed increase in particle faceting with stronger PAW activation as the combined result of faster precursor conversion, increased nucleation rate, shorter growth duration, and possible mild post-nucleation reshaping, rather than as direct evidence of a single facet-selective pathway.

4. Conclusion

This work demonstrates that plasma-activated water can act as a controllable reaction medium for directing gold nanoparticle formation under ambient conditions. By temporally separating atmospheric-pressure plasma treatment from nanoparticle synthesis, the physicochemical properties of plasma-activated water were independently adjusted prior to Au^{3+} reduction, enabling direct correlation between plasma-generated liquid chemistry and nanoparticle formation behaviour. Increasing plasma activation time progressively enriched plasma-activated water with long-lived reactive oxygen species, particularly H_2O_2, while simultaneously lowering pH and increasing oxidation–reduction potential. These changes strongly affected Au^{3+} reduction rates and particle growth behaviour. Strongly activated PAW promoted faster precursor conversion and formation of smaller, more uniform, and more faceted nanoparticles, whereas weakly activated PAW resulted in slower reduction, broader size distributions, and a higher fraction of anisotropic and plate-like morphologies. At 1.00 mM [Au^{3+}], increasing plasma activation from 1 to 16 min reduced the characteristic reduction time from over 100 min to below 10 min and decreased the mean particle size from approximately 120 to 80 nm, while further lowering the precursor concentration to 0.10 mM yielded particles as small as 35 nm. Electron microscopy showed that PAW-mediated synthesis favours faceted and polyhedral morphologies. The observed structural evolution is consistent with a shift from slower growth towards faster nucleation and higher transient supersaturation as the chemical composition of PAW changes with plasma treatment time. Overall, the results show that plasma activation time provides direct experimental control over the liquid-phase conditions governing AuNP formation, enabling reproducible adjustment of nanoparticle size, growth rate, and morphology through plasma-defined solution chemistry.

CRediT authorship contribution statement

Jelena Štrbac: Investigation, Data curation, Visualization, Formal analysis, Methodology, Writing – original draft, Writing – review & editing. **Damjan Vengust:** Investigation, Formal analysis, Visualization, Writing – review & editing. **Janez Zavašnik:** Investigation, Formal analysis, Methodology, Visualization, Writing – review & editing. **James Leon Walsh:** Conceptualization, Validation, Writing – review & editing. **Uroš Cvelbar:** Supervision, Project administration, Resources, Conceptualization, Writing – review & editing, Funding acquisition. **Martina Modic:** Conceptualization, Supervision, Writing – review & editing. **Vasyl Shvalya:** Conceptualization, Formal analysis, Methodology, Data curation, Visualization, Writing – original draft, Writing – review & editing, Funding acquisition, Supervision. Jelena Štrbac and Vasyl Shvalya contributed equally.

Declaration of competing interest

The authors declare that they have no known competing financial interests or personal relationships that could have appeared to influence the work reported in this paper.

Acknowledgement

The authors gratefully acknowledge the financial support of the Slovenian Agency for Research and Innovation (ARIS) within the research program P1-0417 and the projects J2-4490, J2-50066.

Appendix A. Supplementary data

The Supplementary information contains additional reaction schemes, plasma diagnostics, physicochemical considerations related to plasma-activated water and gold nanoparticle faceting, time-resolved UV–Vis measurements, colloidal stability analysis, electron microscopy data, and extended statistical characterization supporting the conclusions of the main manuscript. Supplementary data to this article can be found online at https://doi.org/10.1016/j.matdes.2026.116254.

Data availability

Data will be made available on request.

References

[1] L.W. Chen, Y.C. Hao, J. Li, L. Hu, Y. Guo, S. Li, D. Liu, Z. Zhu, S.Q. Wu, H.Z. Huang, A.X. Yin, B. Wang, Y.W. Zhang, Multi-twinned gold nanoparticles with tensile

surface steps for efficient electrocatalytic CO2 reduction, Sci. China Chem. 65 (2022) 2188–2196, https://doi.org/10.1007/s11426-022-1315-x.
[2] S. Wang, H. Yan, W. Huo, A. Davydok, M. Zając, J. Stępień, H. Feng, Z. Xie, J. K. Shang, P.H.C. Camargo, J. Jiang, F. Fang, Engineering multiple nano-twinned high entropy alloy electrocatalysts toward efficient water electrolysis, Appl. Catal. B Environ. Energy 363 (2025) 124791, https://doi.org/10.1016/j.apcatb.2024.124791.
[3] A. Radoua, M. Romain, E. Chazeau, N. Marthouret, F. Picaud, G. Herlem, C. Goze, N. Millot, O. Micheau, Bioorthogonal click chemistry-mediated conjugation of an anti-DR4 antibody to gold nanorods enhances its pro-apoptotic activity under near infra-red-light stimulation, Mater. Des. 255 (2025) 114212, https://doi.org/10.1016/j.matdes.2025.114212.
[4] H. Liu, F. Xing, Y. Zhou, P. Yu, J. Xu, R. Luo, Z. Xiang, P. Maria Rommens, M. Liu, U. Ritz, Nanomaterials-based photothermal therapies for antibacterial applications, Mater. Des. 233 (2023) 112231, https://doi.org/10.1016/j.matdes.2023.112231.
[5] L. Yao, D. Bojic, M. Liu, Applications and safety of gold nanoparticles as therapeutic devices in clinical trials, J. Pharm. Anal. 13 (2023) 960–967, https://doi.org/10.1016/j.jpha.2023.06.001.
[6] Y. Hang, A. Wang, N. Wu, Plasmonic silver and gold nanoparticles: shape- and structure-modulated plasmonic functionality for point-of-caring sensing, bio-imaging and medical therapy, Chem. Soc. Rev. 53 (2024) 2932–2971, https://doi.org/10.1039/d3cs00793f.
[7] J. Turkevich, P.C. Stevenson, J. Hillier, A study of the nucleation and growth processes in the synthesis of colloidal gold, Discuss. Faraday Soc. 11 (1951) 55–75, https://doi.org/10.1039/df9511100055.
[8] M. Brust, M. Walker, D. Bethell, D.J. Schiffrin, R. Whyman, Synthesis of thiol-derivatised gold nanoparticles in a two-phase liquid-liquid system, J. Chem. Soc. Chem. Commun. (1994) 801–802, https://doi.org/10.1039/c39940000801.
[9] D. Debnath, S.H. Kim, K.E. Geckeler, The first solid-phase route to fabricate and size-tune gold nanoparticles at room temperature, J. Mater. Chem. 19 (2009) 8810–8816, https://doi.org/10.1039/b905260g.
[10] P. Yadav, S.P. Singh, A.K. Rengan, A. Shanavas, R. Srivastava, Gold laced bio-macromolecules for theranostic application, Int. J. Biol. Macromol. 110 (2018) 39–53, https://doi.org/10.1016/j.ijbiomac.2017.10.124.
[11] X. Ma, F. Lin, X. Chen, C. Jin, Unveiling growth pathways of multiply twinned gold nanoparticles by in situ liquid cell transmission electron microscopy, ACS Nano 14 (2020) 9594–9604, https://doi.org/10.1021/acsnano.9b10173.
[12] J. Patel, L. Němcová, P. Maguire, W.G. Graham, D. Mariotti, Synthesis of surfactant-free electrostatically stabilized gold nanoparticles by plasma-induced liquid chemistry, Nanotechnology 24 (2013) 245604, https://doi.org/10.1088/0957-4484/24/24/245604.
[13] D. Čempel, M.T. Nguyen, Y. Ishida, T. Tokunaga, T. Yonezawa, Ligand free green plasma-in-liquid synthesis of Au/Ag alloy nanoparticles, New J. Chem. 42 (2018) 5680–5687, https://doi.org/10.1039/c7nj05154a.
[14] L.N. Nguyen, N. Kaushik, P. Lamichhane, S. Mumtaz, R. Paneru, P. Bhartiya, J. S. Kwon, Y.K. Mishra, L.Q. Nguyen, N.K. Kaushik, E.H. Choi, In situ plasma-assisted synthesis of polydopamine-functionalized gold nanoparticles for biomedical applications, Green Chem. 22 (2020) 6588–6599, https://doi.org/10.1039/d0gc01348j.
[15] H. Liu, K. Ikeda, M.T. Nguyen, S. Sato, N. Matsuda, H. Tsukamoto, T. Tokunaga, T. Yonezawa, Alginate-stabilized gold nanoparticles prepared using the microwave-induced plasma-in-liquid process with long-term storage stability for potential biomedical applications, ACS Omega 7 (2022) 6238–6247, https://doi.org/10.1021/acsomega.1c06769.
[16] N. Khatoon, H.M. Yasin, M. Younus, W. Ahmed, N.U. Rehman, M. Zakaullah, M. Z. Iqbal, Synthesis and spectroscopic characterization of gold nanoparticles via plasma-liquid interaction technique, AIP Adv. 8 (2018) 015314, https://doi.org/10.1063/1.5004470.
[17] X. Liang, Z. Jun Wang, C. Jun Liu, Size-controlled synthesis of colloidal gold nanoparticles at room temperature under the influence of glow discharge, Nanoscale Res. Lett. 5 (2010) 124–129, https://doi.org/10.1007/s11671-009-9453-0.
[18] M. Sanavandi, K. Aalikhani, M. Shafiee, H. Rabbani, G. Fazli, N. Sadeghi, B. Shokri, A one-step plasma assisted synthesis of gold nanoparticles and simultaneous linker-free conjugation with nestin: an in vitro study of cellular toxicity, Nano Lett. 25 (2025) 1974–1983, https://doi.org/10.1021/acs.nanolett.4c05641.
[19] A. Bjelajac, A.M. Phillipe, J. Guillot, Y. Fleming, J.B. Chemin, P. Choquet, S. Bulou, Gold nanoparticles synthesis and immobilization by atmospheric pressure DBD plasma torch method, Nanoscale Adv. 5 (2023) 2573–2582, https://doi.org/10.1039/d3na00007a.
[20] M. Bouchard, M. Laprise-Pelletier, S. Turgeon, M.A. Fortin, Efficient and rapid synthesis of radioactive gold nanoparticles by dielectric barrier discharge, Part. Part. Syst. Charact. 34 (2017) 1600231, https://doi.org/10.1002/ppsc.201600231.
[21] M.A. Bratescu, S.P. Cho, O. Takai, N. Saito, Size-controlled gold nanoparticles synthesized in solution plasma, J. Phys. Chem. C 115 (2011) 24569–24576, https://doi.org/10.1021/jp207447c.
[22] A. Izadi, R.J. Anthony, A plasma-based gas-phase method for synthesis of gold nanoparticles, Plasma Process. Polym. 16 (2019) e1800212, https://doi.org/10.1002/ppap.201800212.
[23] J.H. Nam, G. Nayak, S. Exarhos, C.M. Mueller, D. Xu, G.C. Schatz, P.J. Bruggeman, Mechanisms of controlled stabilizer-free synthesis of gold nanoparticles in liquid aerosol containing plasma, Chem. Sci. 15 (2024) 11643–11656, https://doi.org/10.1039/d4sc01192a.
[24] Q. Chen, J. Li, Y. Li, A review of plasma–liquid interactions for nanomaterial synthesis, J. Phys. D Appl. Phys. 48 (2015) 424005, https://doi.org/10.1088/0022-3727/48/42/424005.
[25] K.S. Wong, N.S.L. Chew, M. Low, M.K. Tan, Plasma-activated water: physicochemical properties, generation techniques, and applications, Processes 11 (2023) 2213, https://doi.org/10.3390/pr11072213.
[26] W.F.L.M. Hoeben, P.P. van Ooij, D.C. Schram, T. Huiskamp, A.J.M. Pemen, P. Lukeš, On the possibilities of straightforward characterization of plasma activated water, Plasma Chem. Plasma Process. 39 (2019) 597–626, https://doi.org/10.1007/s11090-019-09976-7.
[27] J. Julák, A. Hujacová, V. Scholtz, J. Khun, K. Holada, Contribution to the chemistry of plasma-activated water, Plasma Phys. Rep. 44 (2018) 125–136, https://doi.org/10.1134/S1063780X18010075.
[28] R. Montalbetti, Z. Machala, M. Gherardi, R. Laurita, Production and chemical composition of plasma activated water: a systematic review and meta-analysis, Plasma Process. Polym. 22 (2025) 2400249, https://doi.org/10.1002/ppap.202400249.
[29] B. Machado-Moreira, B.K. Tiwari, K.G. Richards, F. Abram, C.M. Burgess, Application of plasma activated water for decontamination of alfalfa and mung bean seeds, Food Microbiol. 96 (2021) 103708, https://doi.org/10.1016/j.fm.2020.103708.
[30] Q. Wang, D. Salvi, Recent progress in the application of plasma-activated water (PAW) for food decontamination, Curr. Opin. Food Sci. 42 (2021) 51–60, https://doi.org/10.1016/j.cofs.2021.04.012.
[31] H.K.N. Vyas, B. Xia, D. Alam, N.P. Gracie, J.G. Rothwell, S.A. Rice, D. Carter, P. J. Cullen, A. Mai-Prochnow, Plasma activated water as a pre-treatment strategy in the context of biofilm-infected chronic wounds, Biofilm 6 (2023) 100154, https://doi.org/10.1016/j.bioflm.2023.100154.
[32] S. Kooshki, P. Pareek, M. Janda, Z. Machala, Selective reactive oxygen and nitrogen species production in plasma-activated water via dielectric barrier discharge reactor: an innovative method for tuning and its impact on dye degradation, J. Water Process Eng. 63 (2024) 105477, https://doi.org/10.1016/j.jwpe.2024.105477.
[33] M. Sahni, B.R. Locke, Quantification of hydroxyl radicals produced in aqueous phase pulsed electrical discharge reactors, Ind. Eng. Chem. Res. 45 (2006) 5819–5825, https://doi.org/10.1021/ie0601504.
[34] R. Dringen, L. Kussmaul, B. Hamprecht, Detoxification of exogenous hydrogen peroxide and organic hydroperoxides by cultured astroglial cells assessed by microtiter plate assay, Int. J. Dev. Neurosci. 16 (1998) 765–773, https://doi.org/10.1016/S0736-5748(98)00054-5.
[35] F.A.J. Armstrong, Determination of nitrate in water by ultraviolet spectrophotometry, Anal. Chem. 35 (1963) 1292–1294, https://doi.org/10.1021/ac60202a036.
[36] R. Kumar, L. Binetti, T.H. Nguyen, L.S.M. Alwis, A. Agrawal, T. Sun, K.T.V. Grattan, Determination of the aspect-ratio distribution of gold nanorods in a colloidal solution using UV-visible absorption spectroscopy, Sci. Rep. 9 (2019) 17468, https://doi.org/10.1038/s41598-019-53621-4.
[37] T. Hendel, M. Wuithschick, F. Kettemann, A. Birnbaum, K. Rademann, J. Polte, In situ determination of colloidal gold concentrations with UV–Vis spectroscopy: limitations and perspectives, Anal. Chem. 86 (2014) 11115–11124, https://doi.org/10.1021/ac502053s.
[38] W. Haiss, N.T.K. Thanh, J. Aveyard, D.G. Fernig, Determination of size and concentration of gold nanoparticles from UV-Vis spectra, Anal. Chem. 79 (2007) 4215–4221, https://doi.org/10.1021/ac0702084.
[39] E. Tomaszewska, K. Soliwoda, K. Kadziola, B. Tkacz-Szczesna, G. Celichowski, M. Cichomski, W. Szmaja, J. Grobelny, Detection limits of DLS and UV-Vis spectroscopy in characterization of polydisperse nanoparticles colloids, J. Nanomater. 2013 (2013) 313081, https://doi.org/10.1155/2013/313081.
[40] J. Olenik, V. Shvalya, M. Modic, D. Vengust, U. Cvelbar, J.L. Walsh, Microplasma controlled nanogold sensor for SERS of aliphatic and aromatic explosives with PCA-KNN recognition, ACS Sens. 10 (2025) 387–397, https://doi.org/10.1021/acssensors.4c02651.
[41] I.E. Vlad, S.D. Anghel, Time stability of water activated by different on-liquid atmospheric pressure plasmas, J. Electrostat. 87 (2017) 284–292, https://doi.org/10.1016/j.elstat.2017.06.002.
[42] P. Rumbach, D.M. Bartels, R.M. Sankaran, D.B. Go, The solvation of electrons by an atmospheric-pressure plasma, Nat. Commun. 6 (2015) 7248, https://doi.org/10.1038/ncomms8248.
[43] D.T. Elg, H.E. Delgado, D.C. Martin, R.M. Sankaran, P. Rumbach, D.M. Bartels, D. B. Go, Recent advances in understanding the role of solvated electrons at the plasma-liquid interface of solution-based gas discharges, Spectrochim. Acta Part B at. Spectrosc. 186 (2021) 106307, https://doi.org/10.1016/j.sab.2021.106307.
[44] P.R. Rotondo, D. Aceto, M. Ambrico, A.M. Stellacci, F. Faretra, R.M. De Miccolis Angelini, P.F. Ambrico, Physicochemical properties of plasma-activated water and associated antimicrobial activity against fungi and bacteria, Sci. Rep. 15 (2025) 88369, https://doi.org/10.1038/s41598-025-88369-7.
[45] A. Copeland, D.A. Lytle, Measuring the oxidation-reduction potential of important oxidants in drinking water, J. Am. Water Works Assoc. 106 (2014) E10–E20, https://doi.org/10.5942/jawwa.2014.106.0002.
[46] N. Tephiruk, S. Homkanchan, J. Puttha, S. Suwannarat, N. Teerakawanich, W. Kanokbannakorn, S. Srisonphan, CO2 reduction and seedling growth enhancement using dual-function gliding arc plasma system, J. Environ. Chem. Eng. 13 (2025) 117567, https://doi.org/10.1016/j.jece.2025.117567.
[47] J.H. Nam, P. Bruggeman, Effect of the pH on the formation of gold nanoparticles enabled by plasma-driven solution electrochemistry, Plasma Process. Polym. 22 (2025) 2400140, https://doi.org/10.1002/ppap.202400140.

[48] M.G. Jasim, H.R. Humud, Reactive species and storage stability of plasma-activated water from Ar + N2 and Ar + O2 DBD systems, Plasma Chem. Plasma Process. 46 (2026) 6, https://doi.org/10.1007/s11090-025-10626-4.
[49] N. Elgrishi, K.J. Rountree, B.D. McCarthy, E.S. Rountree, T.T. Eisenhart, J. L. Dempsey, A practical beginner's guide to cyclic voltammetry, J. Chem. Educ. 95 (2018) 197–206, https://doi.org/10.1021/acs.jchemed.7b00361.
[50] E.J.F. Dickinson, J.G. Limon-Petersen, N.V. Rees, R.G. Compton, How much supporting electrolyte is required to make a cyclic voltammetry experiment quantitatively "diffusional"? a theoretical and experimental investigation, J. Phys. Chem. C 113 (2009) 11157–11171, https://doi.org/10.1021/jp901628h.
[51] K. Pacławski, K. Fitzner, Kinetics of reduction of gold(III) complexes using H2O2, Metall. Mater. Trans. B 37 (2006) 703–714, https://doi.org/10.1007/s11663-006-0054-3.
[52] G. Frens, Controlled nucleation for the regulation of the particle size in monodisperse gold suspensions, Nat. Phys. Sci. 241 (1973) 20–22, https://doi.org/10.1038/physci241020a0.
[53] M.R. Ivanov, H.R. Bednar, A.J. Haes, Investigations of the mechanism of gold nanoparticle stability and surface functionalization in capillary electrophoresis, ACS Nano 3 (2009) 386–394, https://doi.org/10.1021/nn8005619.
[54] L. Scarabelli, M. Coronado-Puchau, J.J. Giner-Casares, J. Langer, L.M. Liz-Marzán, Monodisperse gold nanotriangles: size control, large-scale self-assembly, and performance in surface-enhanced Raman scattering, ACS Nano 8 (2014) 5833–5842, https://doi.org/10.1021/nn500727w.
[55] B.N. Khlebtsov, N.G. Khlebtsov, On the measurement of gold nanoparticle sizes by the dynamic light scattering method, Colloid J. 73 (2011) 118–127, https://doi.org/10.1134/s1061933x11010078.
[56] Y. Song, Y. Li, M. Zhou, H. Li, T. Xu, C. Zhou, F. Ke, D. Huo, Y. Wan, J. Jie, W. W. Xu, M. Zhu, R. Jin, Atomic structure of a seed-sized gold nanoprism, Nat. Commun. 13 (2022) 1235, https://doi.org/10.1038/s41467-022-28829-0.